Aging in a two-dimensional swarmalator crystal with delayed interactions

Chanin Kumpeerakij,[1,2,*] Thiparat Chotibut,[3,4,†] and Oleg Kogan[5,‡]
[1]*Department of Physics, University of Colorado, Boulder, Colorado 80302, USA*
[2]*Interdisciplinary Quantitative Biology Program (IQ Biology), BioFrontiers Institute, University of Colorado, Boulder, Colorado 80302, USA*
[3]*Chula Intelligent and Complex Systems Center of Excellence, Department of Physics, Faculty of Science, Chulalongkorn University, Bangkok, Thailand*
[4]*Siam Quantum Square (SQ^2), Faculty of Science, Chulalongkorn University, Bangkok, Thailand*
[5]*Department of Physics, Queens College of CUNY, Flushing, New York 11367, USA*

(Received 6 August 2025; accepted 6 April 2026; published 26 June 2026)

Time delay can have a significant impact on the properties of collective organization of active matter. In the previous paper [Phys. Rev. E **109**, 014205 (2024)], we discussed delay-induced breathing in a system of swarmalators—a model coupling particles' internal phases to spatial interactions. Here, we build on that study to investigate the aging phenomenon in this system. It is the aging of a two-dimensional crystal with defects and inhomogeneous lattice constants and takes place after the breathing transients subside. We show that aging proceeds through the gradual elimination of fivefold and sevenfold coordination number defects, which merge pairwise or migrate to the cluster boundary, incrementally increasing the hexatic order parameter in the bulk. Despite this process, defects usually do not fully disappear; some residual number of defects remain frozen in the interior. However, we found that it is possible to achieve a nearly total elimination of coordination number defects at sufficiently low delay—when the surface of the cluster develops a sufficeintly thick fluidized "boiling layer." This mechanism of boundary-mediated annealing reveals a nonequilibrium pathway to achieving high crystalline order in the bulk and raises a tantalizing possibility for controlling defects in active matter with free boundaries.

DOI: 10.1103/bx11-ktk3

I. INTRODUCTION

Active matter offers a rich avenue for investigating collective phenomena far from equilibrium. From bacterial colonies to synthetic colloidal suspensions, active particles are continually driven out of equilibrium and can often self-organize into new types of spatiotemporal collective patterns [1–8]. The Landau-Peierls argument, closely related to the Mermin-Wagner theorem for continuous symmetries, predicts that thermal fluctuations destroy true long-range positional order, allowing at best quasi-long-range order [9]. However, in active matter, persistent propulsion, delayed feedback, and nonreciprocal interactions can relax these equilibrium constraints, giving rise to a broader repertoire of collective states, such as active turbulence, hyperuniform order, long-range order in two-dimensional (2D), and nontrivial defect dynamics [10–15]. Investigating how 2D crystallization proceeds under these nonequilibrium conditions remains an active area of research in condensed matter physics.

Within this broader context, the swarmalator model introduced by O'Keeffe, Hong, and Strogatz [6] (OHS model) provides a minimal setting to investigate how active particle positions and internal phase dynamics can coevolve to form out-of-equilibrium collective states. Swarmalators couple swarming (the spatial attraction or repulsion of agents) with dynamics of internal periodic phaselike variables (which allow phase synchronization or antisynchronization), leading to states where the geometric, spatial arrangement and phase alignment become intertwined. Recently, Ref. [16] showed that adding a constant time delay to the phase interaction in the OHS model can produce collective behaviors completely different from those found in the delay-free system.

Time delays capture realistic features of biological systems, where internal signaling cannot be assumed to act instantaneously. One scenario that could lead to delay is the processing of received signals and production of signaling molecules by cells [17]. Another scenario that could plausibly lead to time delay is the chemical signaling of internal cell cycle (phase) between cells—if this information propagates slowly on the time scale of cells' internal phase dynamics. This "light cone" type of delay will depend on the relative positions of cells. In this paper, we consider a simple case of a constant delay, regardless of relative positions—so, it is more fitting to the first scenario.

Our prior work [16] has demonstrated that sufficiently large delays in the phases of the OHS model give rise to a pronounced breathing transient: The entire disk-shaped swarm cluster expands and contracts radially, reminiscent of a breathing mode (see Fig. 1 of Ref. [16]), characterized by a well-defined oscillation frequency and decay rate. After this breathing subsides, depending on the delay time, the

*Contact author: chanin.kumpeerakij@colorado.edu
†Contact author: thiparatc@gmail.com
‡Contact author: oleg.kogan@qc.cuny.edu

Published by the American Physical Society under the terms of the Creative Commons Attribution 4.0 International license. Further distribution of this work must maintain attribution to the author(s) and the published article's title, journal citation, and DOI.

cluster may settle into either what seems like a quiescent state or a dynamic state with persistent boilinglike motions of particles near the boundary. More subtly, even seemingly quiescent clusters exhibit aging dynamics—a slow and long-lived process wherein residual creeping motions gradually nudge particles' positions slightly on ever-longer timescales. Such aging is characterized by the increasingly slow, progressive elimination of local coordination number defects in the swarmalators' arrangement. Thus, aging in swarmalator clusters add to the list of already known glassy relaxation processes observed in other active or soft-matter systems [18–22].

In this work, we study in detail such late-time aging dynamics numerically, revealing the processes by which the fraction of coordination number defects decreases over time. Local changes in coordination numbers, particularly fivefold and sevenfold defects, take place through annihilation, migration, or pair production. Our analysis also shows that when the boiling layer is sufficiently thick, it is possible for the solid core located underneath this layer to be nearly or even completely defect-free.

In passive 2D systems, crystalline melting proceeds via dislocation and disclination unbinding described by Kosterlitz-Thouless-Halperin-Nelson-Young (KTHNY) theory [23–27]. Our active cluster does not melt; it ages toward higher order, so we invoke KTHNY only as a reference language for defect phenomenology. Our system is non-Hamiltonian and has free boundaries that act as a sink for defects. These distinctions place its aging pathway outside the KTHNY framework, akin to the nonequilibrium ordering reported in active Brownian disks and other driven 2D systems [13,28,29].

The remainder of the paper is organized as follows. In Sec. II, we briefly review the delayed swarmalator model and its previously observed long-lived breathing modes. Section III focuses on the slow creep and glassy relaxation that persists long after the breathing has decayed. We show that defect annihilation and migration underlie this aging process, leading to gradually improved hexatic order. In Sec. IV, we study the dependence of the fraction of defects on the quality factor and also discover the possibility of a complete elimination of defects from a solid core underneath the boiling layer. Finally, we conclude in Sec. VI by situating these findings in the larger landscape of nonequilibrium active matter and discussing open directions for future research.

II. SWARMALATORS WITH DELAYED INTERACTIONS

Consider a system of particles in two dimensions with positions $\mathbf{x}$ and internal phases θ that evolve in time according to

$$\dot{\mathbf{x}}_i = \frac{1}{N}\sum_{j\neq i}^{N}\left[\frac{\mathbf{x}_j-\mathbf{x}_i}{|\mathbf{x}_j-\mathbf{x}_i|}(1+J\cos(\theta_j(t-\tau)-\theta_i(t))) - \frac{\mathbf{x}_j-\mathbf{x}_i}{|\mathbf{x}_j-\mathbf{x}_i|^2}\right], \tag{1}$$

$$\dot{\theta}_i = \frac{K}{N}\sum_{j\neq i}^{N}\frac{\sin(\theta_j(t-\tau)-\theta_i(t))}{|\mathbf{x}_j-\mathbf{x}_i|}. \tag{2}$$

Here, τ is the time delay—a particle i responds to the phase of a particle j as it was time τ ago. The parameter J, which is always chosen to be positive, determines the degree to which similarity of phases increases the tendency of two particles to move toward each other. The parameter K is the phase coupling parameter that controls the tendency of particles to align phases. Positive K causes particles to align their phases, while negative K causes antialignment. Overall, Eqs. (1) and (2) describe a two-way feedback between the spatial and phase organization: Relative phases affect spatial dynamics, and spatial positions affect phase dynamics. With τ set to zero, the equations reduce to the O'Keeffe, Hong, and Strogatz model [6]. The role of nonzero τ was studied in Ref. [16]. Before focusing on the long time aging dynamics, we first review the relevant phenomenology introduced by the time delay.

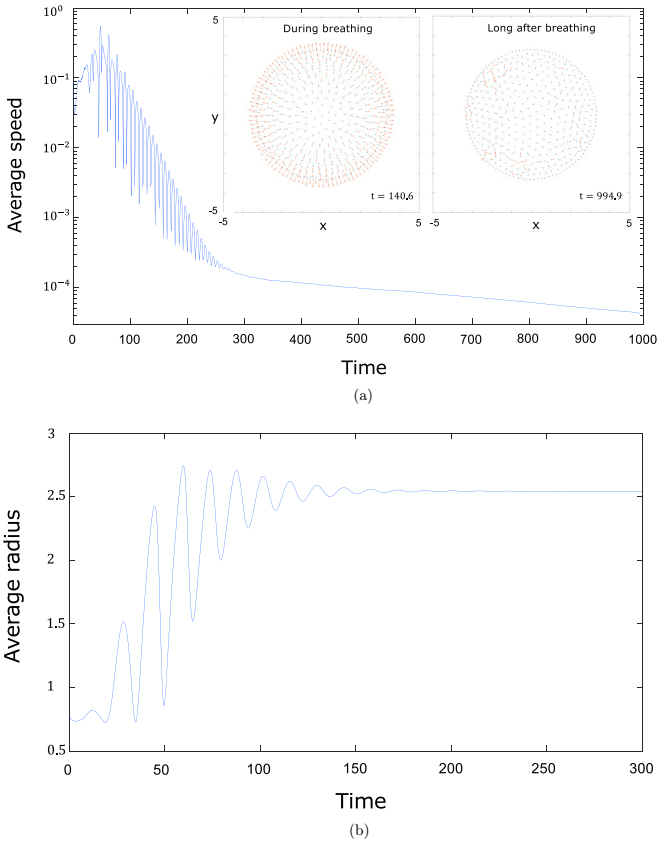


FIG. 1. Breathing transient and the slow creep that follows it—an example. Here, $N = 400$, $J = 1$, $K = -0.75$, and $\tau = 11$. (a) Average speed as a function of time. The breathing behavior ends at $t \approx 300$. Inserts show a velocity pattern: left—expansion during one of the "breaths"; right—during the slow creep (the magnitudes of velocity vectors have been greatly increased for visibility). The centers of clusters were placed at the origin. (b) Average radius as a function of time during breathing.

A. Transient state: Breathing behavior

Following an initial condition, (see Sec. III A of Ref. [16]), the particles undergo a complicated transient, motion. During an early stage of the transient the particles experience spatial rearrangements. With the passage of time, the cluster of particles enters the "breathing behavior" in which the radius of each particle oscillates (see Fig. 1). In the later stages of this breathing behavior, the particles no longer rearrange, i.e., the

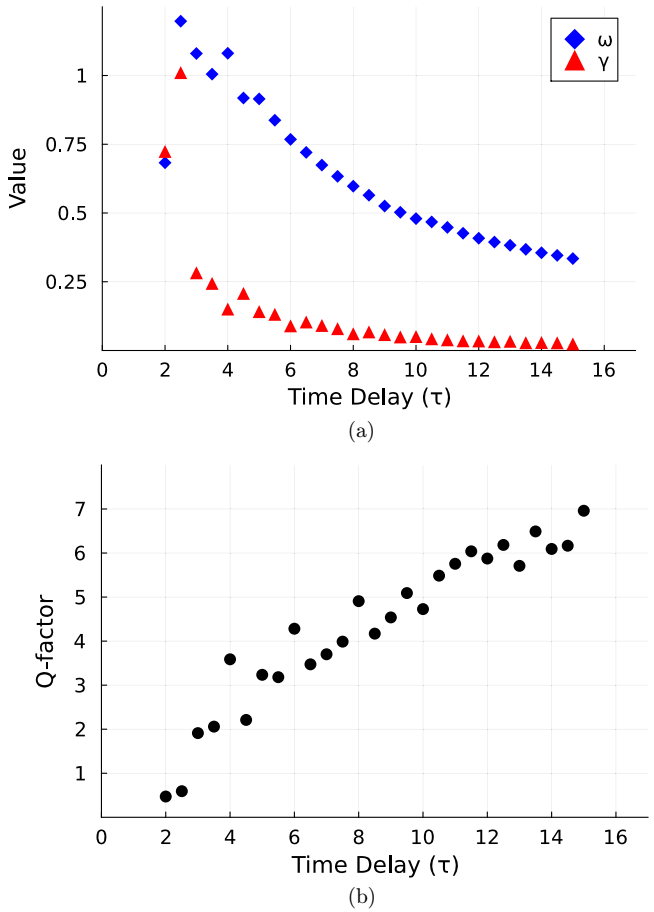


FIG. 2. Properties of breathing oscillations. In this example, the parameters are $N = 1000$, $J = 1.0$, and $K = -0.75$. The lower critical τ is evidently close to 2.0. (a) Angular frequency ω (blue diamonds) and decay rate γ (red triangles) as functions of delay. (b) Quality factor $Q \equiv \frac{\omega}{2\gamma}$ as a function of delay.

identity of neighbors, as defined by Delaunay triangulation, for example, becomes fixed. Figure 2 displays oscillation frequency and decay rate, as well as the quality factor, all as functions of τ. Appendix D discusses how these quantities are extracted from the numerical data. Our prior work that was dedicated to the theory of breathing transients [16] goes into great detail of how such functions can be obtained analytically, once the assumption of no-rearrangements is made. After the breathing decays away, the cluster of particles enters either a boiling state or a quasistatic state, depending on the value of τ [16].

B. Long time phases

In the boiling phase, the cluster of particles separates into two regions—the fluidized boiling layer, where particles are visibly moving in convectivelike motions, and a solid core underneath this fluidized layer, where particles are visibly stationary. This type of phase is found for a sufficiently low delay, below a certain critical value τ_c [16]. On the other hand, for $\tau > \tau_c$, the entire cluster is visibly solid; i.e., there is no boiling layer on the surface. In both cases, the solid part of the cluster is not fully hexagonal—it contains patches of hexagonal crystalline order, but there are defects that make it an imperfect crystal. When we examine the particle velocities on a logarithmic scale for $\tau > \tau_c$, we realize that there are residual velocities—hence, the adjective quasistatic. These velocities undergo certain dynamics, with an overall tendency to decrease in magnitude (see Fig. 1). We go into a detailed description of this aging process in Sec. III.

As τ is lowered below τ_c, the thickness of the boiling layer increases with decreasing τ. Concurrently, the properties of the breathing behavior also change with decreasing τ. Specifically, the frequency ω and decay rate γ of breathing both tend to increase. The decay rate, however, increases faster, so the quality factor of breathing, defined as $Q \equiv \frac{\omega}{2\gamma}$, decreases and eventually tends to zero (the quality factor of an oscillator is a measure of the number of oscillations during a decay time, i.e., it is a characteristic number of oscillations). The quality factor goes to zero at a lower critical delay, which we call τ_l. It appears that the thickness of the boiling layer becomes the entire radius of the cluster around the same τ, and the phases stop synchronizing also around the same τ. We have not studied the details of the latter two processes to identify whether they happen at exactly the same τ, and this will not be addressed in the current paper.

III. AGING DYNAMICS

We now turn our attention to the aging dynamics, which unfolds over timescales much longer than the decay time of the breathing transient. Simulation details pertinent to this and following sections can be found in Appendix A. Aging phenomena, characterized by exceedingly slow structural rearrangements, have been documented across a variety of active matter systems [19–22,30–32]. In active systems, slow relaxation toward crystalline order can proceed via defect-driven dynamics that differ fundamentally from the near-equilibrium mechanisms described by KTHNY theory [13,29,33,34]. Here, we report a slow, incremental defect-healing process that we found in the swarmalator system. As illustrated in Fig. 3, the average particle speed gradually decreases in a nonmonotonic manner, punctuated by occasional increases. When we look at the cluster itself and velocity vectors, we discover that these increases correspond to episodes of increased mobility (velocity "hot spots")associated with localized adjustments of particle positions that generally lead to the change in the local coordination numbers. However, these are very small adjustments, and they do not lead to exchanges of particle positions (i.e., particle rearrangements).

A. Hexatic order parameter

We also examined the local hexatic order parameter (OP), which is defined for each particle j as

$$\Psi(j) = \frac{1}{N_j} \sum_{k=1}^{N_j} e^{6i\theta_k}. \tag{3}$$

The sum is performed over N_j nearest neighbors of particle j; the angle θ_k is between the vector from particle j to its kth

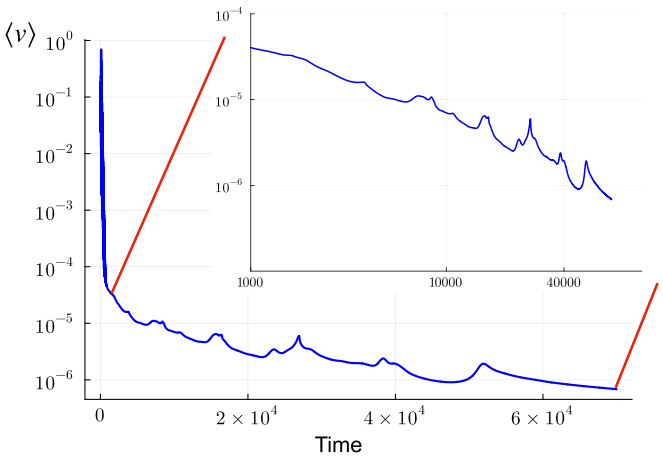


FIG. 3. Average speed over all particles as a function of time. Here, the time span is 2 orders of magnitude longer than the time to complete the breathing (the breathing regime is seen as a vertical drop at the very beginning of the graph; the oscillations are not visible because they finish at time much less than the total time span shown). This plot demonstrates that the relaxation is not uniform when observed over such a long time span, but consists of occasional bursts of increase in the average speed. The parameters are $N = 1000$, $J = 1.0$, $K = -0.75$, and $\tau = 20.0$. Inset: postbreathing dynamics only, displayed on a log-log scale.

neighbor and some chosen reference axis (the "x" axis). The hexatic order parameter is complex, so $\Psi(j) = |\Psi(j)|e^{i\phi(j)}$. A particle surrounded by a perfectly hexagonal arrangement of neighbors will have $|\Psi| = 1$, while six neighbors spaced at unequal angles will lower $|\Psi|$; a particle with coordination number $\neq 6$ will have $|\Psi|$ exactly zero if the angles are equally spaced, and nonzero (but <1) if the angles are not equally spaced. In the remainder of this text, we will occasionally refer to the magnitude of Ψ as "hexaticity."

We display in Fig. 4(b) (middle column) three snapshots of the cluster. On these snapshots, we add velocity vectors to each particle and indicate the magnitude $|\Psi_j|$ with color. The local hexaticity immediately after a velocity hot spot is larger than immediately before it. The velocity hot spots "cure" the local hexaticity. Physically, they correspond to microscopic readjustment of positions that lead to increase of the local hexaticity. We will see below that such positional adjustments can change the identity of neighbors (defined through Delaunay triangulation), but don't involve particle rearrangements.

We visualize the phase part of the local hexatic order parameter in Fig. 4(a) (left-hand column) as arrows that correspond to the argument of $\Psi(j)$, i.e., they depict the complex number $e^{i\phi(j)}$ (we will refer to these as "phase arrows"). Consider, for example, the group of three particles with a low $|\Psi|$ in the lower-right portion of the interior of the cluster. Performing a walk around these three particles in the clockwise direction and completing one revolution, the phase arrows rotate one revolution counterclockwise. This is characteristic of topological charges with value -1. The other group of particles with low $|\Psi|$ in the upper-left portion of the interior have the same property of the phase field around it, also characteristic of topological charges with value -1. On the other hand, it is hard to discern the value of the topological charge of defects located at the edges, since the pattern of phase arrows is too complicated there.

Figure 5 plots on the same timescale the average velocity and the magnitude of the global hexaticity, which we define as average of the local $|\Psi(j)|$ over all particles (i.e., it is the average magnitude of the local hexatic order parameter). We note that while this global hexaticity gradually increases, it does not tend to 1; the system does not reach the perfect global hexatic order.

B. Coordination number defects

Additional insight into the behavior just described comes from examining local coordination numbers. To calculate these numbers, we perform Delaunay triangulation and count the number of nearest neighbors of a given particle. A particle with the number of nearest neighbors not equal to six is considered a coordination number defect. It is a more coarse-grained measure than $|\Psi|$ of that particle, since it is possible to have a $|\Psi| < 1$ with six neighbors if the neighbors are not spread uniformly, angle-wise. We give an example of the coordination number plot for in Fig. 4(c) (right-hand column). We also display in Fig. 6 an example of the time evolution of defect fraction of each type. In general, the defect fraction is defined as the (number of defects)/(number of particles in the bulk); see Appendix C for precise methodology of how defect counting was done—it depends on the presence or absence of the boiling layer. An important part of this process—as explained in this Appendix—is the identification of a boundary that separates the bulk from the surface for $\tau < \tau_c$, or the solid core from the boiling layer for $\tau > \tau_c$.

We found that coordination number defects inside the bulk evolve through specific processes: mergers, production, and migration. Examples of these are displayed in Figs. 7(a)–7(c).

C. Migration to the free surface

While the number of defects in the bulk of the system changes through creation and annihilation processes, migration, on average, results in the transport of defects to the surface, thereby also lowering the defect content in the bulk. Video 1 in the Supplemental Material [35] for $\tau = 20$ and Video 2 in the Supplemental Material [35] for $\tau = 5.5$ make it clear that some defects disappear not through pairwise annihilation, but via migration to the surface in pairs; there is a net drift of defects toward the surface.

The following procedure can be used to measure the relative dominance of each process quantitatively. If defect motion is tracked, the number of crossings of the bulk-surface boundary (such as the red circle in Fig. 4) within a time window Δt can be counted—we call it $f(t)$ (this is proportional to the flux of crossing of this boundary, averaged over this time period). Positive $f(t)$ means that during the time period between t and $t + \Delta t$ there was a net flux out of the bulk through this boundary. The total number of defects in the system at each instant of time $N(t)$ can also be tracked. Let ΔN be the change in the total number of defects inside the bulk during this time window. Negative ΔN means that the number of defects in the bulk has decreased. Then, $c(t) \equiv \Delta N(t) + f(t)$

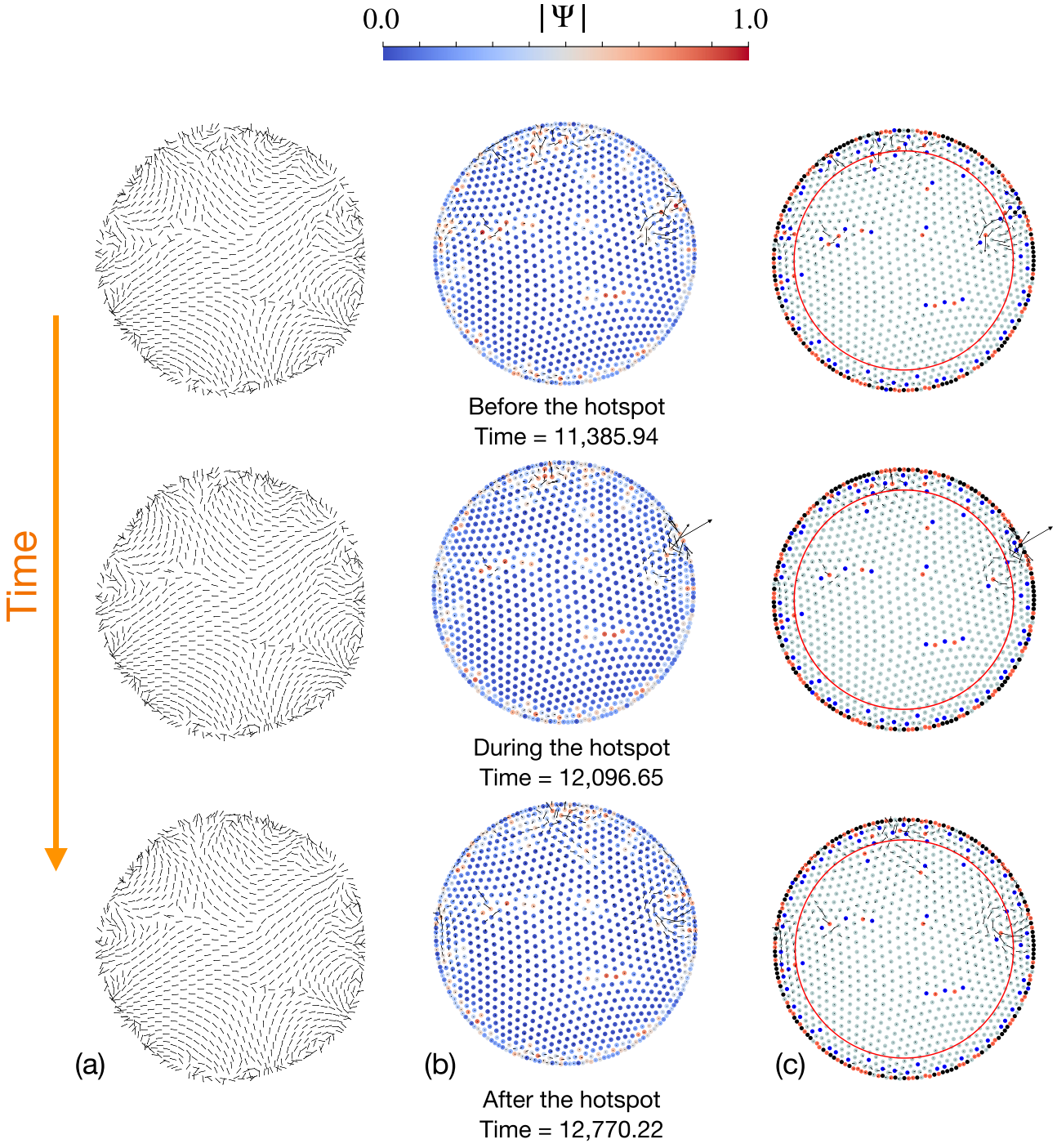


FIG. 4. An example of a time evolution of a system before, during, and after a velocity hot spot. (a) Phase of the local hexatic order parameter. By inspection, we see the presence of topological charges with value −1. (b) Velocity hot spots and magnitude of the local hexatic OP. The color bar represents the scale of absolute magnitude of the local hexatic OP of each particle. (c) Coordination numbers. Orange particles have five nearest neighbors, and blue particles have seven. Particles with six nearest neighbors are in gray, and everything else is black. Here, $N = 1000$, $K = -0.75$, $J = 1.0$, and $\tau = 20.0$. The red circle separates the bulk from the surface, as explained in Appendix C. See Video 1 in the Supplemental Material [35].

is the number of creation events inside the bulk, which is proportional to the time averaged rate of creation of defects inside the bulk. Negative $c(t)$ means that during the said time window more defects were annihilated than created.

Due to the use of variable time-stepping algorithm for solving Eqs. (1) and (2), implementing this procedure with a fixed Δt is difficult in practice. Therefore, we instead tracked changes over a fixed number of time frames (specifically, 500 frames) used in particle tracking. The quantities directly measured are f and N, while c is calculated as above. Details of our procedure for calculating f can be found in Appendix E.

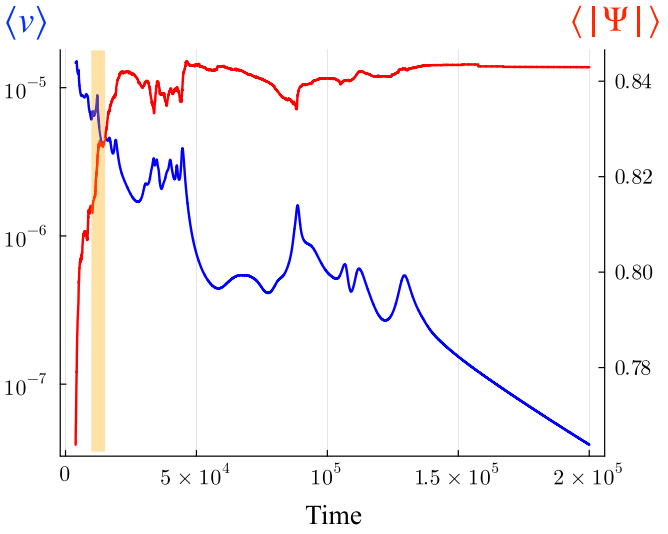


FIG. 5. Evolution of the speed averaged over all particles (blue, decreasing curve), and the local hexaticity averaged over all particles (red, increasing curve). The highlighted window of time corresponds to Fig. 4. Note the uptick in the average speed during that time window. Here, $N = 1000$, $J = 1.0$, $K = -0.75$, and $\tau = 20.0$.

We plot $c(t)$ and $f(t)$ obtained this way in Fig. 8 (the results are expressed as a function of time since we know the relation between the time frame and time). This figure demonstrates that while at earlier times the defect annihilation rate in the bulk is greater than the rate of leaving the bulk into the surface, this process of defect migration to the surface dominates at later times.

IV. DEFECT-FREE SUBSYSTEMS

The aging was discovered in our prior work [16], when we analyzed velocities and found that there is residual creeping motion left after the breathing transient. Our study here revealed the mechanism of this aging process—gradual elimination of coordination number defects by means of mergers

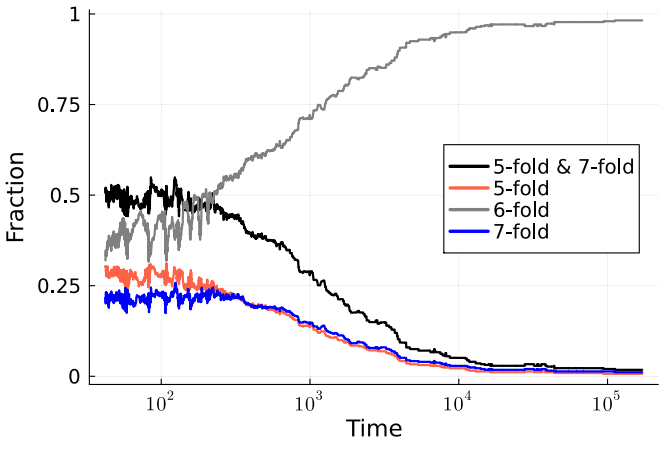


FIG. 6. Evolution of the fraction of particles that have coordination numbers 5 (defect, orange), 6 (black), and 7 (defect, blue). The black curve shows the fraction of particles that constitute either 5- or 7-defects. Here, $N = 1000$, $J = 1.0$, $K = -0.75$, and $\tau = 20.0$.

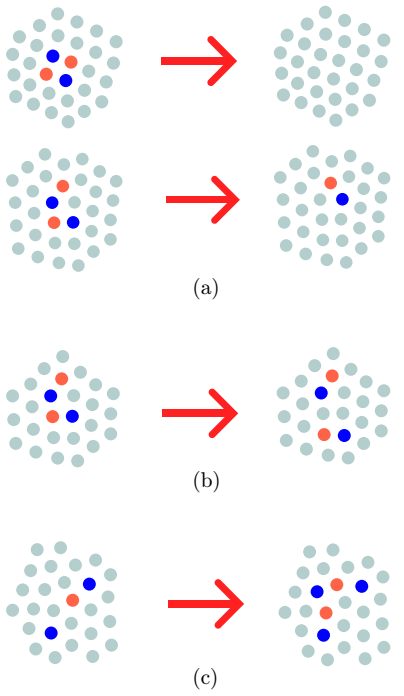


FIG. 7. Defect processes—mergers, migration, and pair creation; (a) Process 1—mergers. In the top panel, we display a double merger—two 5-defects and two 7-defects merge and annihilate each other. In the bottom panel, we display a merger in which there are two pairs of 5- and 7-defects before the merger, and one pair after the merger. (b) Process 2—migration. Here, we display two sets of defect pairs migrating. (c) Process 3—pair production. This is the time reverse of a merger and involves a production of a pair of 5- and 7-defects.

and migration events. However, we found that such defects—and their gradual decrease through these processes—is not unique to a delayed system that displays breathing. In fact, similar dynamics happen for the undelayed system, and even for pure swarmers that have no phase degrees of freedom at all (that corresponds to the $K = 0$ case here). This latter system's evolution is just overdamped dynamics in a potential landscape. More in-depth study of aging phenomenology in other parts of the (J, K) parameter space, including the $J = 0$ swarm-only case, can be found in Sec. V.

We wanted to see if breathing transients that are specific to the delayed swarmalator system causes the system to self-anneal during the breathing stage; whether repeated expansion-contraction cycles give the cluster opportunity to rearrange more effectively during the transient, ultimately lowering the final density of defects in the bulk. To test this hypothesis, we measured the the final defect fraction as a function of the quality factor (which is effectively a measure of the number of oscillations during the breathing stage).

Since Q depends on τ, we performed simulations of system with different delays. For each τ, we simulated systems with 20 different random initial configurations in both spatial positions of particles and their phases. Note that a Q value is not always the same for each τ, and the final defect fraction was also not the same, as both depend on the initial configuration (the role of initial conditions was briefly studied in Sec. 9.1

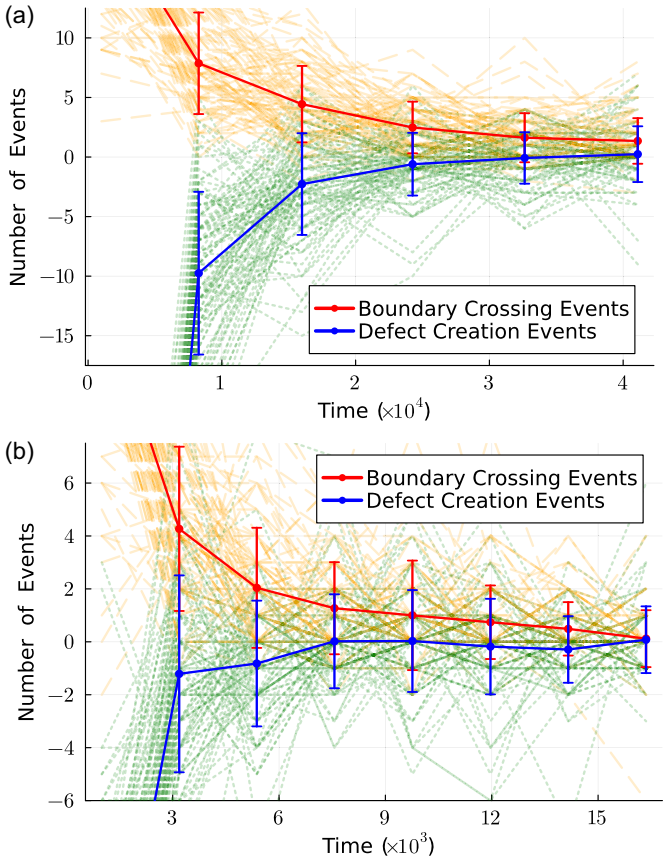


FIG. 8. Number of defect creation or annihilation events, and number of events of crossing out of the bulk and into the surface. Each data point corresponds to the number of events over a 500 time frame window. Here, (a) $\tau = 20 > \tau_c$ and (b) $\tau = 5.5 < \tau_c$, with $J = 1$ and $K = -0.75$ for both. Panel (a) does not show the first pair of dots, which would occur at 21 ± 7.0 and -97 ± 15, rounded to two significant figures; for panel (b), the first pair of dots would occur at 13 ± 5.5 and -16 ± 8.0.

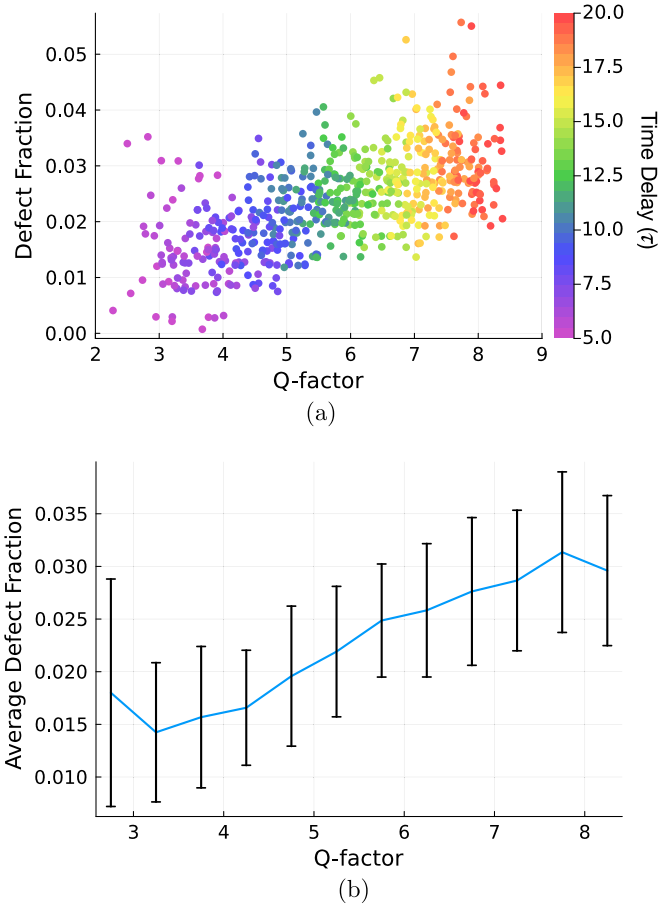


FIG. 9. Dependence of the fraction of defects (computed according to the method described in Appendix C3) on the quality factor of the breathing during the transient. The parameters are $N = 1000$, $J = 1$, and $K = -0.75$. For these parameters, $\tau_c \approx 13$. (a) Defect fraction vs Q factor. One dot per initial condition. Simulations were done for 20 initial conditions per each τ, which ranged between 5 and 20 in steps of 0.5. The lowest defect fraction in this plot is 0.0007. (b) Average and standard deviation computed over bins of size $\Delta Q = 0.5$, from $Q = 2.5$ to $Q = 9$.

of Ref. [36]). The result of this investigation is presented in Fig. 9. The details of the computational procedure that went into generating these results can be found in Appendix C. We are forced to conclude that there does not seem to be an obvious support for the self-annealement hypothesis. The final fraction of defects shows the trend opposite of what we would expect if the self-annealement hypothesis held true; the fraction of defects decreases with decreasing quality factor. In fact, at lower Q values, completely defect-free examples could be found after a long-enough wait; these happen for τ sufficiently below τ_c, in which there is a substantial boiling layer, with a solid core underneath. Fig. 10 shows an example of such a cluster. This complete expulsion of defects appears to be subject to fluctuations; as the boiling layer perturbs the solid core below, the defects exchange between the two layers (see Video 2 in the Supplemental Material [35] for $\tau = 5.5$). The boundary of the solid core is a matter of computational convention (see Appendix C 2), and it may be possible for defects to occasionally cross this conventional boundary in both directions. Therefore, the lower-τ part of Fig. 9 will somewhat depend on the simulation time.

V. CHANGES THROUGHOUT THE (J, K) PLANE

The results presented so far concerned mainly the (J, K) combination located in the corner of the "active phase wave" parameter region of the OHS model [6]; it is here that deep breathing transients take place when phase delay is introduced. We now discuss the situation in other regions of this parameter space. The distinction must be made between transients—such as breathing and long-term behavior—such as the slow aging process during which the average velocity slowly decreases. While the nature of transient behaviors can vary throughout the (J, K) plane, aging—the focus of this paper—is quite common in many other regions of this parameter space. For example, the fourth quadrant displays very long and deep aging, in which the average velocity continues to decrease for many decades. The same can be said for $(J = 0, K > 0)$, in which the spatial dynamics is decoupled from the phase dynamics (thus, the spatial dynamics is a pure swarm). In most of the locations in the (J, K) space that exhibit aging, there are also 5- and 7-defects, which

also undergo creation, annihilation, and migration processes. The difference, however, is in the final defect structure. A common final structure that we found throughout the (J, K) space consists of long, stringlike line of defects frozen in the system, qualitatively similar to defect grain boundary reported in Ref. [28]. In other words, there is less of a tendency for defects to migrate toward the boundary. This appears to be correlated with the structure of the density profile. While the density at $(J = 1, K = -0.75)$ is lower at the center of the cluster, and higher at the surface (see Ref. [16] for the analytical derivation of this profile), this is not the case, for example, in the first or the fourth quadrant—where the density instead is higher in the center. Thus, it suggests that defects tend to migrate down the density gradient.

The following are two examples of aging in other parts of the (J, K) parameter space: fourth quadrant $(J = -0.5, K = 0.5)$ with $\tau = 20$ (Video 3 in the Supplemental Material [35]) and along the positive K axis $(J = 0, K = 0.5$; Video 4 in the Supplemental Material [35]), where the spatial dynamics is decoupled from the phase dynamics, corresponding to pure swarm. Both examples demonstrate the final state with stringlike defect structures. We also looked in the first and third quadrants (by changing the signs of J or K from the first example) and examined $\tau = 5.5$ and $\tau = 20$ in all cases considered. The final states always exhibited qualitatively similar stringlike defect structures.

VI. DISCUSSION

In this paper, we have picked up one of the unanswered questions from our prior work [16]—what is the nature of the slow creep that occurs after the breathing has ceased? We now understand the answer—it is the aging dynamics of the system that takes place through a gradual elimination of coordination number defects. In fact, we found that this aging happens not only above τ_c, but even in the solid cluster below τ_c. It is a process that unfolds on timescales much greater than the breathing period or decay timescale of the transient.

Annihilation occurs between defect pairs, specifically between a 7-defect and a 5-defect. The same can be said for creation—new defects are born in pairs of a 5-defect and a 7-defect. If there is a group consisting of three 7-defects and two 5-defects, the total defect excess is $+1$—and it remains $+1$ if there are annihilation or creation events in that group, based on our observations. Therefore, the defect excess of a group of defects is a conserved quantity. Based on the existence of such a conserved quantity, as well as the structure of the phase of the local hexatic order parameter around defects (which tend to occur in groups), these coordination number defects appear to be topological.

Our study has raised deeper questions that remain unanswered. First, what is the effective interaction between the defects? Second, what triggers annihilation and creation events? For example, does creation of a pair of defects (5 and 7) require another existing defect in the neighborhood? This appears to be the case, but a clear answer requires a statistical study of many defect creation events. If a nearby defect is indeed required, is there an effective strainlike quantity that causes the creation of a pair of defects? We also reported a gradual migration of defects to the surface of the cluster.

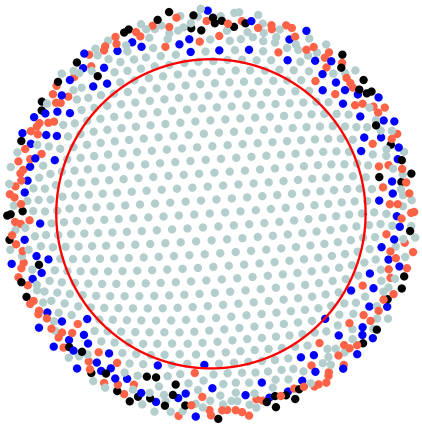


FIG. 10. Example of a defect-free solid core, where the surface develops a fluidized boiling layer. Here, $N = 1000$, $J = 1.0$, $K = -0.75$, and $\tau = 5.5$. This snapshot was taken at $t = 70\,000$; see Video 2 in the Supplemental Material [35] for the complete dynamics starting from $t = 0$.

What is the effective force that pushes defect pairs toward the surface? We found that when there is a thick boiling layer for τ sufficiently below τ_c, it is possible to catch a system with no defects such as in Fig. 10. A tantalizing research question is whether the existence of a "soft" outer layer that facilitates the removal of defects from the solid core presents a unique strategy for perfect crystallization in other active matter systems; is it possible to engineer active particle interactions which cause the formation of a layer that absorbs defects, while leaving other parts of the system defect-free? Going back to the swarmalator system specifically, it is also an interesting question whether it is in principle possible to end up with a defect-free system for $\tau > \tau_c$—perhaps for some very special initial condition? Finally, it is also worth asking what might happen on much longer time scales and for bigger systems. All these questions emerged as we delved into the problem posed in the previous paper [16].

We now put our work in a broader perspective. We provided an example of a two-dimensional nonequilibrium system that ages by means of a gradual elimination of topological defects via mutual annihilation and migration to the boundaries. We mentioned that aging by elimination of defects happens also in a nondelayed model, and even in a basic swarm. Aging via mutual defect annihilation is known to occur in other systems as well. Coarsening processes that involve mutual annihilation of topological defects—typically vortices and antivortices—have been reported in nematic liquid crystals [37], the XY model [38], ferromagnetic superfluids [39], active fluids made from Quincke rollers [40], two-dimensional complex Ginzburg-Landau equation [41,42], and even in a system of Kuramoto oscillators [43]. A system that shares a significant overlap with the phenomenology of our model is described in the recent work by Digregorio *et al.*[28], which proposed a unified analysis of passive and active repulsive Brownian disk systems in two dimensions. Their framework is specific to power-law interactions, which required a box to confine the particles. Our system has all-to-all attractions, and power-law repulsions; therefore, it forms a cluster that does not require a box. The class of systems

considered in Ref. [28] is based on potential with or without an additional active force; our system is non-Hamiltonian.

We pause here to reflect on the significance of boundaries. In addition to defect-defect annihilation, which does take place in all of the aforementioned sources during the aging process—our system also allows expulsion of defects into boundaries. We saw that for a delay below τ_c, the boundary develops a fluidized boiling layer—and a sufficiently thick boiling layer allows a complete absorption of defects, leaving the solid core defect-free. This finding appears quite unique to soft-matter and dynamical systems, although reminiscent processes occur in irradiated materials at high temperature [44–47], where grain boundaries, surfaces, and dislocation cores can serve as sinks for defects (see also a different system here [48]). However, the similarity here may be superficial, due to these systems being rather different from ours. The complete elimination of defects resulting from the interplay of the free boundary and delayed dynamics calls for further search of similar behavior in other models. If this phenomenon could be generalized to other systems—perhaps also requiring delayed dynamics—it could pave way for a mechanism of constructing defect-free materials and systems of active particles.

ACKNOWLEDGMENTS

The authors gratefully acknowledge useful discussions on defect dynamics with David R. Nelson and Leticia Cugliandolo. T.C. acknowledges the funding support from the NSRF via the Program Management Unit for Human Resources & Institutional Development, Research and Innovation (Grant No. B39G690073) and from Thailand Science research and Innovation Fund Chulalongkorn University (IND_FF_69_-258_2300_062). C.K. acknowledges the funding support in part by the Interdisciplinary Quantitative Biology (IQ Biology) Ph.D. program at the BioFrontiers Institute, University of Colorado Boulder, and the National Science Foundation NRT Integrated Data Science Fellowship (Award No. 2022138). O.K. acknowledges startup funds provided by Queens College, City University of New York. The authors used OpenAI ChatGPT for assistance with wording, structural editing, and conceptual clarity; all substantive content is the authors' own.

DATA AVAILABILITY

GitHub link for our code is provided in Ref. [49].

APPENDIX A: NUMERICAL SIMULATION DETAILS

All of the simulations in this article have been done using Julia programming, with the exception of Fig. 1, which was done using **dde23** in Matlab. In Julia, we mainly use the differential equation solver package, *DifferentialEquations.jl*, to solve delayed differential equations. The algorithm that we used to solve the differential equation is **Tsit5** or Runge-Kutta Pairs of Orders 5(4) [50]. In addition, we fixed the random seed while exploring the effect of varying a given parameter. This process initialized the system at the same initial conditions and allowed us to observe the effect of varying each parameter on the system. The exception concerns results in Fig. 9, where 20 different random seeds (20 different initial conditions) were used per τ.

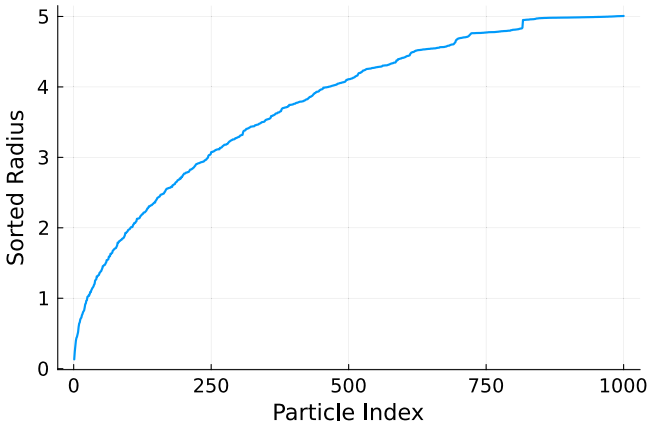


FIG. 11. Sorted particle radii for $N = 1000$, $K = -0.75$, $J = 1.0$, and $\tau = 20$.

APPENDIX B: TESSELATION PROCEDURE

To evaluate the hexatic order parameter Ψ_j of particle j, we first identify its nearest neighbors using the Delaunay triangulation algorithm [51]. This approach ensures a well-defined local connectivity based on spatial proximity. Next, we compute the angles between the horizontal axis and the vectors connecting particle j to each of its neighbors k, using the two-argument arctangent function *atan2*, which is natively available in Julia programming. These angles are then used in the computation of the order parameter via Eq. (3).

APPENDIX C: PROCESS TO COUNT THE NUMBER OF DEFECTS

The method of counting defects differs depending on whether the system is in the boiling ($\tau < \tau_c$) or in the quasistatic ($\tau > \tau_c$) regime. Being in the quasistatic phase allows for a direct evaluation of the bulk radius and defect count within it. Conversely, boiling regime is characterized by persistent (mostly radial) motion of particles in the outer annulus of the system, with a solid core below. Defects only have a meaning in the solid core, so we must estimate its radius.

1. Bulk radius

This procedure was used for $\tau > \tau_c$. Figure 11 is the plot of the radius of each particle in a 1000-particle system. The reason for the specific form of this plot is the following. We showed in Ref. [16] that the density (number of particles per area) follows closely the relationship $(1 - r/R)^{-1/2}$. Thus, close to the center, the density is approximately constant [16], so the number of particles n within a radius should scale like r^2 or $r \propto \sqrt{n}$. Closer to the edge of the cluster (at radius R), the density rapidly grows, so the plot should become horizontal. In addition, due to the discrete nature of particles and their interactions, they organize into ring structures, which is especially prominent near the edge (see, for instance, Fig. 3 in Ref. [16]). For this reason, the radius vs the particle number displays steplike features for r close to R, with the biggest

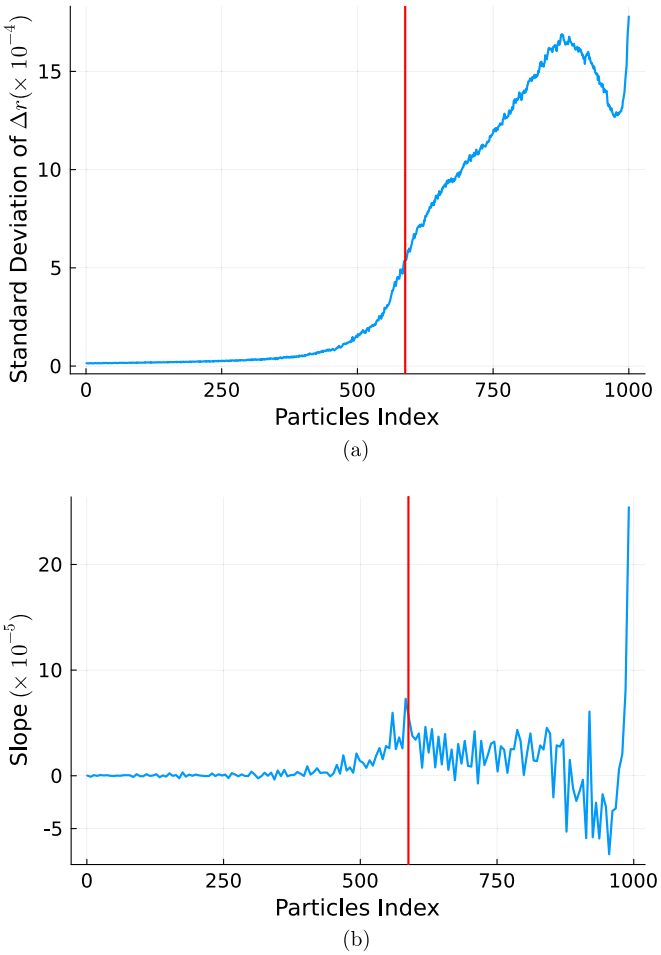


FIG. 12. Calculation of the solid core radius—an example, (a) Standard deviation of Δr over a time series, as a function of particle index. In this figure, we use $N = 1000$, $J = 1.0$, $K = -0.75$, and $\tau = 5.0$. The red vertical line is the location of the calculated solid core radius (while the reported value is 85% of it). (b) Six-point estimate of the slope of std(Δr) vs particle index. The red vertical line is the location of the calculated solid core radius (while the reported value is 85% of it).

jump at the last ring. This was used to identify the bulk. We computed the slope of radius vs particle index function and found the radius at which the slope is greatest—this is the transition to the last step—the outer ring or the "crust" of the cluster. We used 85% of this value as the criterion for the bulk radius. This particular process has been applied the same way in every setup with a quasistatic state.

2. Solid core

When the system is in the boiling state for $\tau < \tau_c$, we need to identify the solid core, which lies below the fluidized layer. To do this, we implemented the following algorithm at the last 5000 time steps of the simulation: (1) at each time step, we sort particle radii, (2) we measure the difference between two consecutive time steps, Δr, and (3) we obtain a time series of Δr over the last 4999 time steps of the simulation and compute the standard deviation over this time series as a function of the particle index; an example is displayed in

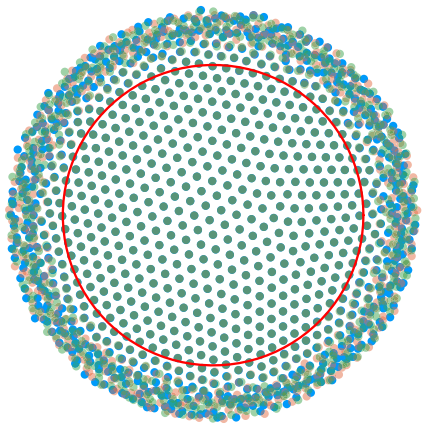


FIG. 13. Superposition of multiple snapshots (in different colors) in the boiling state, showing the fluctuations in the boiling layer, and stable structure that forms the solid core. The red circle represents the estimated bulk radius, which is 85% of the radius corresponding to the red line in Fig. 12; it is the result of the procedure outline in Appendix C2. Here, the parameters are $N = 1000$, $J = 1.0$, $K = -0.75$, and $\tau = 5.0$.

Fig. 12. We are interested in the index at which this function has the largest slope. Measuring local slopes, however, tends to amplify small fluctuations and did not always give an accurate prediction of the solid core radius. Thus, (4) we measured the slope over six points (effectively, an average over six neighboring local slopes) and sought the location at which this locally averaged slope attains a maximum (and related it to radius).

As in the case of the bulk radius estimation, we report 85% of the value obtained with the described algorithm. From our experience, this whole procedure gave an accurate assessment of the radius of the solid core. An example is given in Fig. 13. We found that a step in the radius vs the particle index that we use to identify the bulk radius for $\tau > \tau_c$ actually persists for τ somewhat below τ_c.

For (J, K) parameters that were used to construct Fig. 9 (when $\tau_c \approx 13$), this step persists down to $\tau \approx 9$. We found this by checking that using the solid core procedure between these τ values produces essentially the same boundary. So, we used the bulk radius procedure above this τ and a solid core radius estimation below it. This gave us accurate estimations of the solid core, with a faster computation.

3. Calculating the defect fraction

Defect fraction is defined as the number of defects in the solid core or within the bulk radius divided by the number of particles in the solid core (or within the bulk radius respectively). The defect fraction decreases over time before stabilizing at a plateau above τ_c. In the boiling regime (below τ_c), there are residual fluctuations (see Video 2 of the Supplemental Material [35] for $\tau = 5.5$). To estimate the final defect fraction, we use the following protocol. We compute the average and standard deviation of the defect fraction over a sufficiently long interval near the end of the simulation well beyond the onset of the aging phase. Based on these statistics, we define a tolerance band (visualized as a horizontal colored

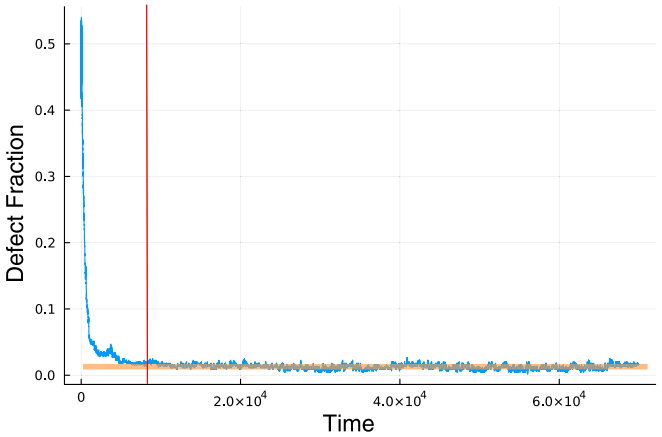


FIG. 14. Defect fraction over time, an example. The horizontal yellow band denotes the range of fluctuations of the defect fraction within one standard deviation at late times. The defect fraction as a function of time first enters this band at the time denoted by the vertical red line. The reported final defect fraction is average over the subsequent 500 time steps. In this example, $N = 1000$, $J = 1.0$, $K = -0.75$, and $\tau = 5.5$.

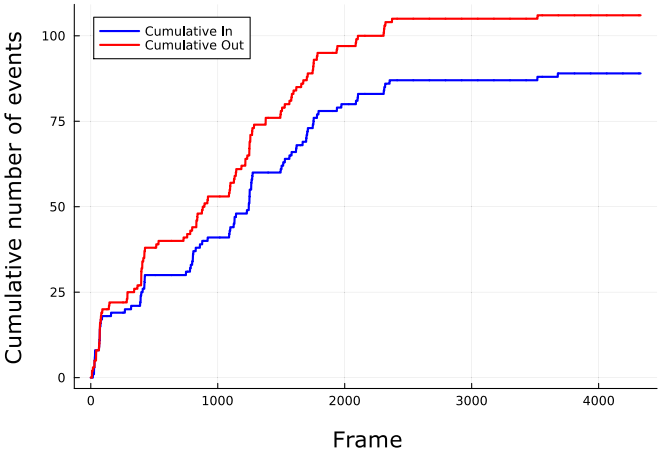


FIG. 15. Cumulative defect crossings at the bulk boundary. While $C_{\text{in}}(t)$ and $C_{\text{out}}(t)$ exhibit steady increases over time due to persistent crossing fluctuations across the boundary, their difference, $C_{\text{net}}(t)$ [defined in Eq. (E1)], reveals the net directional migration of defects from the bulk interior to the exterior.

band in Fig. 14) and locate the earliest time at which the defect fraction enters this band (vertical red line in Fig. 14). From this point onward, we average the defect fraction over the subsequent 500 time steps to reduce statistical fluctuations and obtain an estimate of the final defect fraction value.

APPENDIX D: EXTRACTING THE QUALITY FACTOR

To estimate the quality factor of the breathing oscillation, we fit the radius vs time with a functional form for a damped harmonic oscillator

$$R(t) = Ae^{-\gamma t}\sin(\omega t + \phi) + B. \tag{D1}$$

Initially, the algorithm fits the entire dataset using Eq. (D1). It then computes the mean squared error (MSE) between the fitted curve and the empirical data. If the MSE exceeds a predefined threshold, the algorithm iteratively shortens the fitting interval from the beginning of the time series. This strategy is motivated by the observation that the swarmalator system exhibits chaotic behavior before transitioning into a coherent breathing phase. The iterative trimming continues until the breathing state is isolated and a satisfactory fit is achieved. Once optimal fitting parameters are obtained, the quality factor Q, which characterizes the number of oscillations during one decay time, is calculated as $Q = \omega/(2\gamma)$.

APPENDIX E: CALCULATING THE DEFECT FLUX OUT OF THE BULK

To quantify the dynamics of the coordination number defects, we developed a multistep tracking protocol. The spatial distribution of defects was first rendered as a time-ordered sequence of images, which were subsequently processed using the Fiji image processing software [52]. We employed the TrackMate plugin to perform automated tracking of individual defects across the temporal sequence [53], yielding high-resolution trajectories of defect positions (x, y) over time.

From these trajectories, we computed the radial distance of each defect from the system's center of mass. We define $C_{\text{out}}(t)$ and $C_{\text{in}}(t)$ as the cumulative number of defects that have migrated from interior to the exterior and vice versa—with the dividing circle identified with the procedure described in Appendix C. The net number of defects that crossed from the bulk into the surface, $f(t)$, is then calculated by measuring the change in the net crossing count over a fixed interval of $\Delta k = 500$ frames:

$$C_{\text{net}}(t) = C_{\text{out}}(t) - C_{\text{in}}(t), \tag{E1}$$

$$f(t) = C_{\text{net}}(t + \Delta t) - C_{\text{net}}(t), \tag{E2}$$

where Δt corresponds to the physical time elapsed over the 500-frame window; see Fig. 15. Because our numerical solver utilizes an adaptive time-stepping scheme, we define this interval by a constant number of frames rather than a fixed temporal duration to ensure consistent statistical sampling of the defect trajectories.

[1] S. Ramaswamy, The mechanics and statistics of active matter, Annu. Rev. Condens. Matter Phys. **1**, 323 (2010).

[2] M. C. Marchetti, J.-F. Joanny, S. Ramaswamy, T. B. Liverpool, J. Prost, M. Rao, and R. A. Simha, Hydrodynamics of soft active matter, Rev. Mod. Phys. **85**, 1143 (2013).

[3] T. Vicsek and A. Zafeiris, Collective motion, Phys. Rep. **517**, 71 (2012).

[4] G. Gompper, R. G. Winkler, T. Speck, A. Solon, C. Nardini, F. Peruani, H. Löwen, R. Golestanian, U. B. Kaupp, L. Alvarez, T. Kiørboe, E. Lauga, W. C. K. Poon, A. DeSimone, P. L.

Muiño, J. M. Yeomans, A. Doostmohammadi, T. N. Shendruk, M. Arroyo, and D. Marenduzzo, The 2020 motile active matter roadmap, J. Phys.: Condens. Matter **32**, 193001 (2020).

[5] M. R. Shaebani, A. Wysocki, R. G. Winkler, G. Gompper, and H. Rieger, Computational models for active matter, Nat. Rev. Phys. **2**, 181 (2020).

[6] K. P. O'Keeffe, H. Hong, and S. H. Strogatz, Oscillators that sync and swarm, Nat. Commun. **8**, 1504 (2017).

[7] M. J. Bowick, N. Fakhri, M. C. Marchetti, and S. Ramaswamy, Symmetry, thermodynamics, and topology in active matter, Phys. Rev. X **12**, 010501 (2022).

[8] S. Shankar, A. Souslov, M. J. Bowick, M. C. Marchetti, and V. Vitelli, Topological active matter, Nat. Rev. Phys. **4**, 380 (2022).

[9] L. D. Landau and E. M. Lifshitz, *Statistical Physics, Part 1* (Butterworth-Heinemann, Oxford, 1980), 3rd ed.

[10] M. Fruchart, Y. Zhou, and V. Vitelli, Nonreciprocal phase transitions, Nature (London) **592**, 363 (2021).

[11] A. Doostmohammadi, M. F. Adamer, S. P. Thampi, and J. M. Yeomans, Stabilization of active matter by flow-vortex lattices and defect ordering, Nat. Commun. **7**, 10557 (2016).

[12] H. H. Wensink, J. Dunkel, S. Heidenreich, K. Drescher, R. E. Goldstein, H. Löwen, and J. M. Yeomans, Meso-scale turbulence in living fluids, Proc. Natl. Acad. Sci. USA **109**, 14308 (2012).

[13] V. Soni, L. R. Gómez, and W. T. M. Irvine, Emergent geometry of inhomogeneous planar crystals, Phys. Rev. X **8**, 011039 (2018).

[14] J. H. Weijs, R. Jeanneret, R. Dreyfus, and D. Bartolo, Emergent hyperuniformity in periodically driven emulsions, Proc. Natl. Acad. Sci. USA **112**, E7035 (2015).

[15] J. Toner and Y. Tu, Flocks, herds, and schools: A quantitative theory of flocking, Phys. Rev. E **58**, 4828 (1998).

[16] N. Blum, A. Li, K. O'Keeffe, and O. Kogan, Swarmalators with delayed interactions, Phys. Rev. E **109**, 014205 (2024).

[17] G. Petrungaro, L. G. Morelli, and K. Uriu, Information flow in the presence of cell mixing and signaling delays during embryonic development, in *Seminars in Cell & Developmental Biology* (Elsevier, London, UK, 2019), Vol. 93, pp. 26–35.

[18] L. Berthier and J. Kurchan, Non-equilibrium glass transitions in driven and active matter, Nat. Phys. **9**, 310 (2013).

[19] K. Paul, A. Mutneja, S. K. Nandi, and S. Karmakar, Dynamical heterogeneity in active glasses is inherently different from its equilibrium behavior, Proc. Natl. Acad. Sci. USA **120**, e2217073120 (2023).

[20] L. Cipelletti, L. Ramos, S. Manley, E. Pitard, D. Weitz, E. Pashkovski, and M. Johansson, Universal non-diffusive slow dynamics in aging soft matter, Faraday Discuss. **123**, 237 (2003).

[21] L. M. Janssen, A. Kaiser, and H. Löwen, Aging and rejuvenation of active matter under topological constraints, Sci. Rep. **7**, 5667 (2017).

[22] L. Berthier, E. Flenner, and G. Szamel, Glassy dynamics in dense systems of active particles, J. Chem. Phys. **150**, 200901 (2019).

[23] J. M. Kosterlitz and D. J. Thouless, Long range order and metastability in two dimensional solids and superfluids. (Application of dislocation theory), J. Phys. C **5**, L124 (1972).

[24] J. M. Kosterlitz and D. J. Thouless, Ordering, metastability and phase transitions in two-dimensional systems, J. Phys. C **6**, 1181 (1973).

[25] B. I. Halperin and D. R. Nelson, Theory of two-dimensional melting, Phys. Rev. Lett. **41**, 121 (1978).

[26] D. R. Nelson and B. I. Halperin, Dislocation-mediated melting in two dimensions, Phys. Rev. B **19**, 2457 (1979).

[27] A. P. Young, Melting and the vector Coulomb gas in two dimensions, Phys. Rev. B **19**, 1855 (1979).

[28] P. Digregorio, D. Levis, L. F. Cugliandolo, G. Gonnella, and I. Pagonabarraga, Unified analysis of topological defects in 2D systems of active and passive disks, Soft Matter **18**, 566 (2022).

[29] L. Galliano, M. E. Cates, and L. Berthier, Two-dimensional crystals far from equilibrium, Phys. Rev. Lett. **131**, 047101 (2023).

[30] M. Paoluzzi, D. Levis, and I. Pagonabarraga, From flocking to glassiness in dense disordered polar active matter, Commun. Phys. **7**, 57 (2024).

[31] G. Janzen and L. M. C. Janssen, Aging in thermal active glasses, Phys. Rev. Res. **4**, L012038 (2022).

[32] G. Janzen and L. M. C. Janssen, Rejuvenation and memory effects in active glasses induced by thermal and active cycling, Phys. Rev. Res. **6**, 023257 (2024).

[33] P. Digregorio, D. Levis, A. Suma, L. F. Cugliandolo, G. Gonnella, and I. Pagonabarraga, Full phase diagram of active Brownian disks: From melting to motility-induced phase separation, Phys. Rev. Lett. **121**, 098003 (2018).

[34] R. Singh and R. Adhikari, Universal hydrodynamic mechanisms for crystallization in active colloidal suspensions, Phys. Rev. Lett. **117**, 228002 (2016).

[35] See Supplemental Material at http://link.aps.org/supplemental/10.1103/bx11-ktk3 for a collection of videos that shows the dynamical behavior of the system.

[36] N. S. Blum, Swarming oscillators with time-delayed interactions, 2021, https://digitalcommons.calpoly.edu/physsp/205/.

[37] I. Chuang, B. Yurke, A. N. Pargellis, and N. Turok, Coarsening dynamics in uniaxial nematic liquid crystals, Phys. Rev. E **47**, 3343 (1993).

[38] B. Yurke, A. N. Pargellis, T. Kovacs, and D. A. Huse, Coarsening dynamics of the XY model, Phys. Rev. E **47**, 1525 (1993).

[39] L. Williamson and B. Blackie, Anomalous phase ordering of a quenched ferromagnetic superfluid, SciPost Phys. **7**, 029 (2019).

[40] A. Chardac, S. Shankar, M. C. Marchetti, and D. Bartolo, Emergence of dynamic vortex glasses in disordered polar active fluids, Proc. Natl. Acad. Sci. USA **118**, e2018218118 (2021).

[41] W. Liu and U. C. Täuber, Aging phenomena in the two-dimensional complex Ginzburg-Landau equation, Europhys. Lett. **128**, 30006 (2020).

[42] M. Arnold and R. Nigmatullin, Dynamics of vortex defect formation in two-dimensional Coulomb crystals, Phys. Rev. B **106**, 104106 (2022).

[43] Y. Rouzaire and D. Levis, Dynamics of topological defects in the noisy Kuramoto model in two dimensions, Front. Phys. **10**, 976515 (2022).

[44] C. Hung, G. Vetterick, E. Hopkins, J. Balwin, P. Baldo, M. Kirk, A. Misra, and M. Taheri, Insight into defect cluster annihilation at grain boundaries in an irradiated nanocrystalline iron, J. Nucl. Mater. **566**, 153761 (2022).

[45] A. Aitkaliyeva, L. He, H. Wen, B. Miller, X.-M. Bai, and T. Allen, Irradiation effects in generation IV nuclear reactor materials, in *Structural Materials for Generation IV Nuclear Reactors*, edited by P. Yvon (Elsevier, Cambridge, 2017), pp. 253–283.

[46] R. Zheng, L. Yang, and L. Zhang, Grain boundary migration as a self-healing mechanism of tungsten at high temperature, Metals **12**, 1491 (2022).

[47] N. V. Doan and G. Martin, Elimination of irradiation point defects in crystalline solids: Sink strengths, Phys. Rev. B **67**, 134107 (2003).

[48] S. J. Gerbode, U. Agarwal, D. C. Ong, C. M. Liddell, F. Escobedo, and I. Cohen, Glassy dislocation dynamics in 2D colloidal dimer crystals, Phys. Rev. Lett. **105**, 078301 (2010).

[49] C. Kumpeerakij, Delayed interaction swarmalator, 2025, https://github.com/chku-ucb/delayed-interaction-swarmalator (see "Readme" file for more details).

[50] C. Tsitouras, Runge-Kutta pairs of orders 5(4) using the minimal set of simplifying assumptions, AIP Conf. Proc. **1168**, 69 (2009).

[51] S.-W. Cheng, T. K. Dey, and J. Shewchuk, *Delaunay Mesh Generation*, Chapman & Hall/CRC Computer & Information Science Series (Chapman & Hall/CRC, Philadelphia, PA, 2009).

[52] J. Schindelin, I. Arganda-Carreras, E. Frise, V. Kaynig, M. Longair, T. Pietzsch, S. Preibisch, C. Rueden, S. Saalfeld, B. Schmid, J.-Y. Tinevez, D. J. White, V. Hartenstein, K. Eliceiri, P. Tomancak, and A. Cardona, Fiji: An open-source platform for biological-image analysis, Nat. Methods **9**, 676 (2012).

[53] D. Ershov, M.-S. Phan, J. W. Pylvänäinen, S. U. Rigaud, L. Le Blanc, A. Charles-Orszag, J. R. W. Conway, R. F. Laine, N. H. Roy, D. Bonazzi, G. Duménil, G. Jacquemet, and J.-Y. Tinevez, TrackMate 7: integrating state-of-the-art segmentation algorithms into tracking pipelines, Nat Methods **19**, 829 (2022).